Ordered arrays of embedded Ga nanoparticles on patterned silicon substrates

M Bollani[1], S Bietti[2], C Frigeri[3], D Chrastina[4], K Reyes[5], P Smereka[5], J M Millunchick[6], G M Vanacore[7,9], M Burghammer[8], A Tagliaferri[7] and S Sanguinetti[2]

[1] CNR-IFN, L-NESS, via Anzani 42, I-22100 Como, Italy
[2] L-NESS, Dip. Scienza dei Materiali, Univ. Milano Bicocca, via Cozzi 53, I-20155 Milano, Italy
[3] CNR-IMEM, Parco Area delle Scienze, 37/A, I-43124 Parma, Italy
[4] L-NESS, Dip. di Fisica, Politecnico di Milano, via Anzani 42, I-22100 Como, Italy
[5] Department of Mathematics, University of Michigan, Ann Arbor, MI, USA
[6] Department of Materials Science and Engineering, University of Michigan, Ann Arbor, MI, USA
[7] CNISM and Dipartimento di Fisica, Politecnico di Milano, Piazza Leonardo da Vinci, I-32-20133 Milano, Italy
[8] European Synchrotron Radiation Facility, BP 220, F-38043 Grenoble Cedex, France

9 Present address: Physical Biology Center for Ultrafast Science and Technology, Arthur Amos Noyes Laboratory of Chemical Physics, California Institute of Technology, Pasadena, CA 91125, USA.
E-mail: stefano.sanguinetti@unimib.it

Received 24 January 2014, revised 17 March 2014
Accepted for publication 24 March 2014
Published 30 April 2014

Localized surface plasmon resonances (LSPRs) in metal nanoparticles (NPs) deposited on semiconductors can promote absorption, strong optical scattering, and a strongly enhanced optical near-field around the particle [1]. The enhanced optical scattering properties of LSPRs allow for the development of advanced light trapping concepts in the visible–near infrared range, which are relevant in case of photodetectors or photovoltaic devices based on thin films or low absorbing materials, such as Si [2–5]. An alternative use of LSPR to enhance absorption performance has been proposed, in which photons are absorbed directly in the metal NPs, generating 'hot' energetic electrons (or holes), that can then be extracted from the metal via internal photoemission across a metal–semiconductor Schottky junction [6–9]. In such a twofold framework for absorption enhancement (enhanced scattering and internal photoemission), metal NPs embedded in the semiconductor material act with higher efficiency, with respect to surface deposited NPs [10–12]. However, no reliable method for the fabrication of embedded metal NPs has yet been reported in the literature.

The fabrication of metallic NPs organized in ordered arrays on the surface would allow for better NP size and density control and uniformity, in view of a fully scalable and reproducible device engineering approach. Usually metal NPs are prepared over large areas via the simple process of dewetting a thin solid metal film on a flat substrate [5, 6, 13–15]. Unfortunately, the dewetting process results in metal islands with broad distributions of sizes and spacings. Particles of near-uniform size can be achieved through the use of topographically patterned substrates for the NP assembly [16, 17]. In addition substrate patterning can be used to achieve a controlled positioning of the NPs, thus opening the path to complex design of surface plasma resonances in the more suitable energy ranges for the application in view [13–15].

In this letter we show that site-controlled, ordered arrays of embedded metallic NPs can be fabricated on patterned Si substrates, allowing for NP size and density control. The embedded NP growth process has been investigated through a combination of extensive chemical and structural characterization supported by theoretical kinetic Monte Carlo (KMC) simulations. The metal chosen in our approach is Ga. Even if plasmonics research has focused nearly exclusively on Ag and Au NPs, Ga-based plasmonics is gaining an increasing interest, due to the strong design possibility offered by the Ga LSPR. In particular, it has been shown that the LSPR of Ga NPs can be tuned over the wide range of 0.8 to 5.8 eV. This can be achieved by NP diameter control in the 10–300 nm range [18–22]. In addition, Ga is highly compatible with standard microelectronics processes, and highly controlled deposition Ga methods are widely available.

Our growth procedure for the fabrication of the ordered array of embedded Ga NPs is based on a combination of substrate patterning and droplet epitaxy growth [23, 24]. There are three steps involved in the process: (i) a patterned Si surface is prepared with an ordered array of inverted pyramid pits to provide preferential nucleation sites for the metallic Ga droplets; (ii) metallic Ga droplets are obtained on the patterned Si surface via self-assembly from an atomic beam supplied in a molecular-beam epitaxy (MBE) environment; (iii) the sample is submitted to a short pulse of As to promote the surface crystallization of the Ga droplets, thus producing GaAs islands with metallic Ga cores [25–27]. The two MBE steps, which decouple Ga and As deposition, are fundamental to this process as they allow for a strong control of the NP placement and a fine control of the transformation of metallic Ga droplets into embedded Ga NPs.

Ga deposited on Si at typical MBE growth temperatures of 300–600 °C spontaneously self-assembles into a spatially disordered ensemble of nanoscale droplets, whose density and size can be tuned through Ga adatom flux and substrate temperature [28, 29]. In order to promote Ga droplet ordering on the Si substrate we used a periodically modulated two-dimensional inverted pyramid pit patterned substrate which demonstrated the ability to produce almost perfectly ordered arrays of self-assembled islands with high size homogeneity [30–32]. A two-dimensional pit array with a period of 2 μm, aligned along the <110> directions, was patterned by electron beam lithography (EBL) on a Si(001) substrate. EBL was used to define openings in a SiN_x mask, and pits with {111} sidewalls were produced by anisotropic wet etching in tetramethylammonium hydroxide (TMAH) at 80 °C for 4 min [33]. The width, and thus, the depth of these pits were determined by size of the openings. For the samples reported in this work, the typical size of the pits after etching was 525×525 nm^2 base area for a corresponding depth of 360 nm (figure 1). After the removal of the patterned SiN_x film by phosphoric acid, the substrates were cleaned by a standard RCA treatment. The samples were then dipped in a diluted hydrofluoric acid solution to create a hydrogen terminated surface before loading into the MBE system. The substrate temperature was then raised to 780 °C for hydrogen desorption, as confirmed by the change in the surface (2×1) and (1×2) reconstruction observed from reflection high-energy electron diffraction (RHEED). The substrate temperature was then decreased to 510 °C and the background As pressure decreased below 10^{-9} Torr for the deposition of the Ga. 5 MLs of Ga were deposited at a rate of 0.08 ML s^{-1}. Finally, the substrate temperature was decreased to 150 °C and the As cell valve was opened to 7×10^{-5} Torr As beam equivalent pressure for 5 min.

Figure 1 shows a scanning electron microscopy image of a typical array of fully etched inverted {111} pits on a Si(001) substrate surface before and after MBE growth. Well defined NPs are present at the bottom of each pit. No additional NP are nucleated on the flat areas between the pits or on the sidewalls of the pits. On the flat areas around the pattern the Ga NPs are randomly nucleated. From several similar images, it was found that 80% of the pits contained a Ga NP. The procedure of NP localization therefore demonstrates high reproducibility and reliability.

Ga droplets are nucleated at the bottom of the pit due to the combined action of capillarity and Ga adatom diffusion. As a matter of fact, the force that drives the nucleation of the Ga droplet within the pits is provided by the more efficient decrease, respect to the planar substrates, of the droplet nucleation work that takes place in presence of cavities. This phenomenon takes the name of capillarity condensation [34]. Since the activation energy for nucleation on such sites is considerably lowered, and because the nucleation rate can change drastically by small variations of nucleation work, in practice droplets are formed only at the bottom of the pits, if such cavities are within the diffusion range of the Ga adatoms deposited on the solid flat surface.

Thus, the presence of capillarity condensation effects, while providing the necessary free energy advantage to the Ga adatom system for the nucleation of a droplet at the bottom of the pit, does not *per se* guarantee the achievement of this goal. Ga droplet nucleation kinetics should be taken into account in order to prevent unwanted droplet nucleation on the flat areas between the pits and on the pit facets. This can be achieved if the average distance between self-assembled Ga droplets is, on Si(001), of the order of the pit spacing and, on Si(111), larger than the pit facet length. Because these data are unavailable in literature, we determined the actual Ga droplet density on the Si(001) and Si(111) flat surfaces with a series

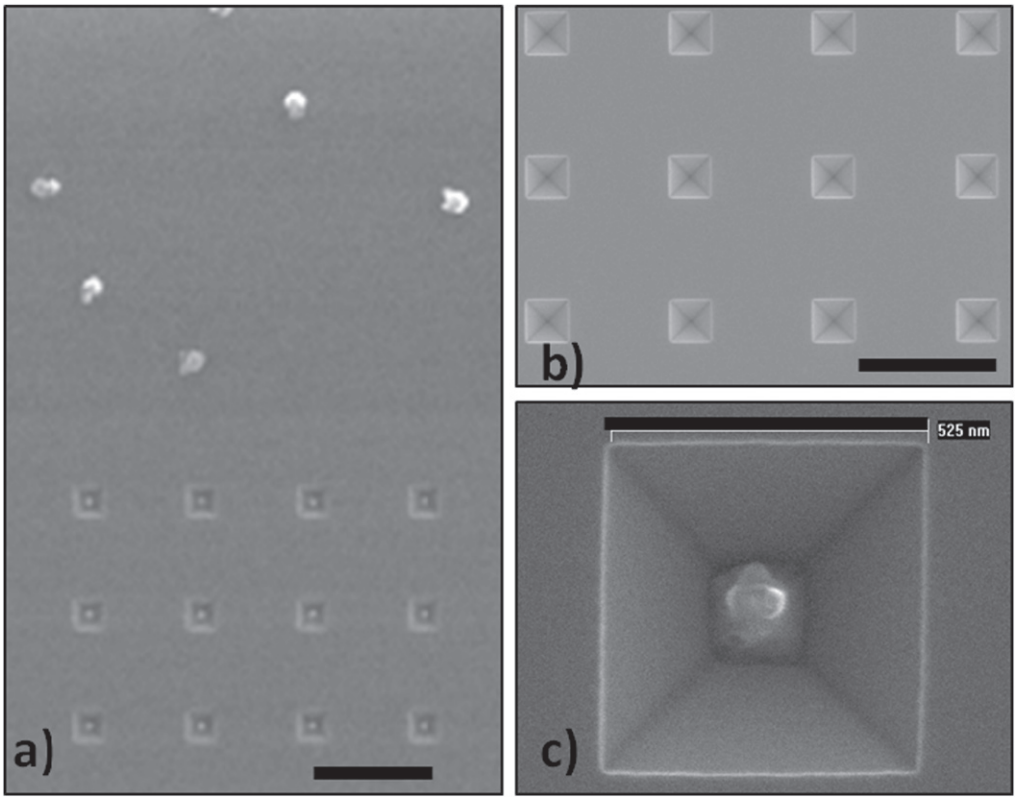

Figure 1. Scanning electron microscopy (SEM) image after deposition of Ga nanoparticles on a prepatterned Si(001) substrate in comparison to Ga nucleation on a flat Si surface (a). After lithography and etching steps, the pits have a pyramid shape with {111} sidewalls (b). High resolution SEM image of a single Ga particle embedded in a pit and covered by a GaAs shell (c). In (a) and (b) the scale bar is 2 μm, while in (c) the scale bar indicates the pit width of 525 nm.

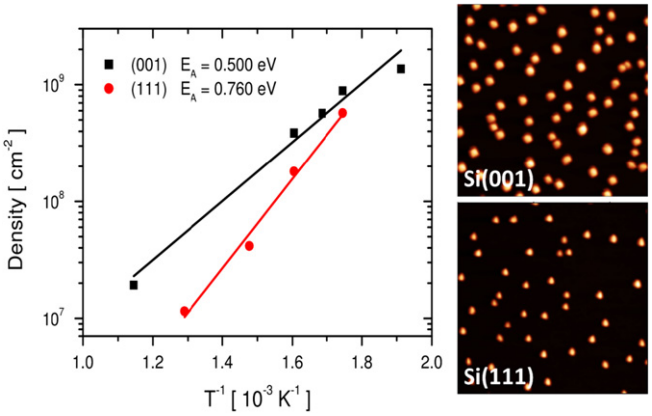

Figure 2. Left panel: density of Ga droplets formed on Si(001) and on Si(111) substrates as a function of inverse Ga deposition temperature $1/T$. Above approximately 270 °C ($1/T \approx 1.85 \times 10^{-3}$ 1/K), droplets are formed more densely on the (001) surface. Right panel: AFM images ($5 \times 5\ \mu m^2$) of droplets formed on Si(001) (top) and Si(111) (bottom) at 350 °C.

of samples in which Ga droplets were deposited at different substrate temperatures in the range 250–600 °C, while keeping fixed the Ga flux (5 MLs of Ga at a rate of 0.08 ML s^{-1}). In figure 2, the droplet density as a function of deposition temperature is reported. Higher substrate temperatures lead to a lower areal density of larger droplets. The temperature dependence follows an exponential law, as expected by activated diffusion and nucleation processes [35], with an activation energy $E_a^{(001)} = 0.50$ eV and $E_a^{(111)} = 0.76$ eV, for Si (001) and Si(111), respectively.

The reported droplet density activation energies well compare with what reported for Ga on GaAs substrate deposition, where $E_a^{(111)} > E_a^{(001)}$ was also observed [36]. However, on the contrary of what we see in Ga/Si, in the Ga/GaAs system the (111) substrates show a higher droplet density, respect to (001) in the whole growth temperature range [36]. Such difference should be traced in the droplet density and density activation energies dependence on the details of Ga diffusion and Ga droplet nucleation dynamics (critical nucleus size, energy and thermal stability) [35, 37] which are expected to differ in the two systems.

The pit pitch of 2.0 μm, thus requiring a density of droplets of 2.5×10^7 cm^{-2}, sets the deposition temperature above 500 °C (see figure 2). Being the {111} pit facet length around 500 nm, such Ga deposition temperature permits to avoid droplet nucleation on the pit sidewalls too. It is worth mentioning that the pit arrangement (distance, depth, topology) is a fully designable parameter in our approach, thus permitting the fabrication on purpose of the NP array. A change in the pit geometry requires in turn a change in the Ga deposition conditions, which have to be adapted to the new pattern. A change in the Ga droplet size can be obtained by varying the total amount of deposited Ga.

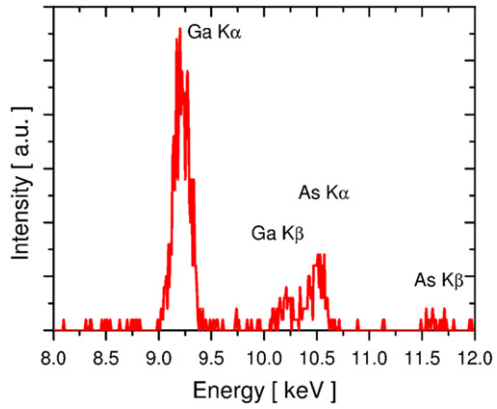

Figure 3. X-ray fluorescence signals (collected normal to the sample surface, with the incoming 15.25 keV x-ray beam at ∼16° to the sample surface) from a Ga droplet nucleated at the base of a {111} pit. The small size of the droplet means that corrections for the absorption of As emission by Ga are negligible, so the relative intensities of the emission lines are directly proportional to the relative amounts of Ga and As in the droplet.

The As deposition step transforms the Ga droplets into GaAs islands [24, 28, 29]. Here the As deposition step is performed under growth conditions where only a partial crystallization of the Ga to GaAs at the droplet surface is obtained, so promoting the formation of Ga NP inclusions within a GaAs matrix as recently observed on flat GaAs(001) surfaces [25, 27]. This transforms each Ga droplet nucleated at the bottom of a pit into an embedded Ga NP. We examined the chemical composition of the droplets after the As supply step by x-ray fluorescence (XRF) (beam energy 15.25 keV) at the ID13 beamline of the European Synchrotron Radiation Facility, observing the K emission lines of Ga and As with a Vortex Si drift detector while scanning the nanofocused x-ray beam (width ∼100 nm) over the array of droplets [38]. Figure 3 shows Ga and As Kα and Kβ emission intensities for a NP at the bottom of a pit after As supply. The NPs are much smaller than the attenuation length of the exciting and emitted x-rays (tens of micrometers [39]) so self-absorption and secondary excitation can be neglected. Thus the average Ga:As ratio within the islands can be directly estimated by considering the ratio of Ga Kα and As Kα emission intensities. Using the cross sections for fluorescence at 15 keV, which are 54.31 $cm^2\,g^{-1}$ for Ga Kα, and 68.57 $cm^2\,g^{-1}$ for As Kα [40] and the density of GaAs according to their relative atomic masses (pure Ga and As are both only slightly denser than GaAs), an As:Ga ratio of approximately 0.2:0.8 was found in the NPs within pits. This clearly shows that the NPs at the bottom of the pits are extremely Ga-rich compared to a stoichiometric composition of Ga and As.

In order to obtain data on the spatial distribution of Ga and As within the NPs, cross-sectional transmission electron microscopy (TEM) was employed to examine the morphology and composition of the NPs at the bottom of the pits. Measurements were performed in a TEM-STEM (scanning-TEM) JEOL 2200 FS machine operated at 200 kV and equipped with a standard energy-dispersive x-ray (EDX) spectrometer. EDX elemental maps were acquired using an STEM spot size of 0.7 nm. The <110> cross sectional specimens were mechanically prepared in a standard way starting from a sandwich containing a piece of sample. For the final thinning an Ar ion beam was used. Figure 4(a) shows the <110> cross sectional STEM image of an NP at the bottom of a pit, obtained by using a HAADF (high angle annular dark field) detector, while Figures 5(b) and (c) show the corresponding EDX maps of the characteristic x-ray Kα emission lines of Ga and As, respectively. EDX maps clearly show that the Ga fills the bottom part of the pit completely, while As is detected only on top of the Ga NP. Quantitative evaluation of the average concentration in the whole area of the As map where the As emission is visible gives 75.45 at% for Ga and 24.55 at% for As. The As and Ga signals are nearly equal only at the top of the NP. A localized exact quantification profile of the Ga and As concentrations within the NP has been obtained by using spectra extracted from the maps at discrete points from narrow areas (size ∼25 nm) along the vertical axis of the pit as shown by the dotted line in figure 4(a). The results are shown in figure 4(d): at the top of the NP the Ga and As concentrations are 52.4 at% and 47.6 at% respectively, i.e. almost stoichiometric. However, the As concentration drops very quickly on descending into the NP, to a value of only 1.9 at%, and this value in maintained throughout the NP. Therefore, most of the NP is almost pure (98.1 at%) Ga.

XRF and TEM characterization both indicate that a Ga-rich embedded NP is formed in the pit. To clarify the distribution of As in the Ga droplet, the nanostructural evolution of growth on patterned silicon substrates was studied using KMC simulations. The model used was extended from that in [24], which studied similar growth methods on a GaAs substrate, by incorporating a Si species. Ga and As bonds to Si are set to be nominally small to capture the non-interactions between Si and the other components. The initial surface is a 1 + 1 dimensional inverted silicon pit of dimensions similar to those of the experimental pits. Ga is deposited until the desired thickness is achieved. We observed in KMC simulations a sufficiently large diffusion length of Ga on Si to allow for a Ga droplet to nucleate at the bottom of the pit. The Ga droplet is then exposed to an As flux. Simulations show (figure 5) that this results in a Ga droplet covered by a thin GaAs shell, rather than a fully crystallized GaAs NP.

Reyes *et al* [26] showed that there are three important processes in the crystallization of Ga droplets under an As overpressure. The first is solidification of the crystal at the vapor–liquid–solid junction, followed by advancement of the solidification front through the droplet. The second process is wicking of the liquid out of the droplet to wet the surface away from the droplet. Both processes are apparent in these simulations. However, due to the choice of bond strengths, the contact angles of the nucleated GaAs cluster on both the Si-vapor and Si-Ga interfaces is large, resulting in only a small amount of wetting of the Si interfaces by GaAs, inhibiting solidification along them. This results in hemispherical growth emanating from clusters in quasi-static growth conditions. The apparent asymmetry of this growth resulting in the formation of a GaAs shell over a metallic core stems from

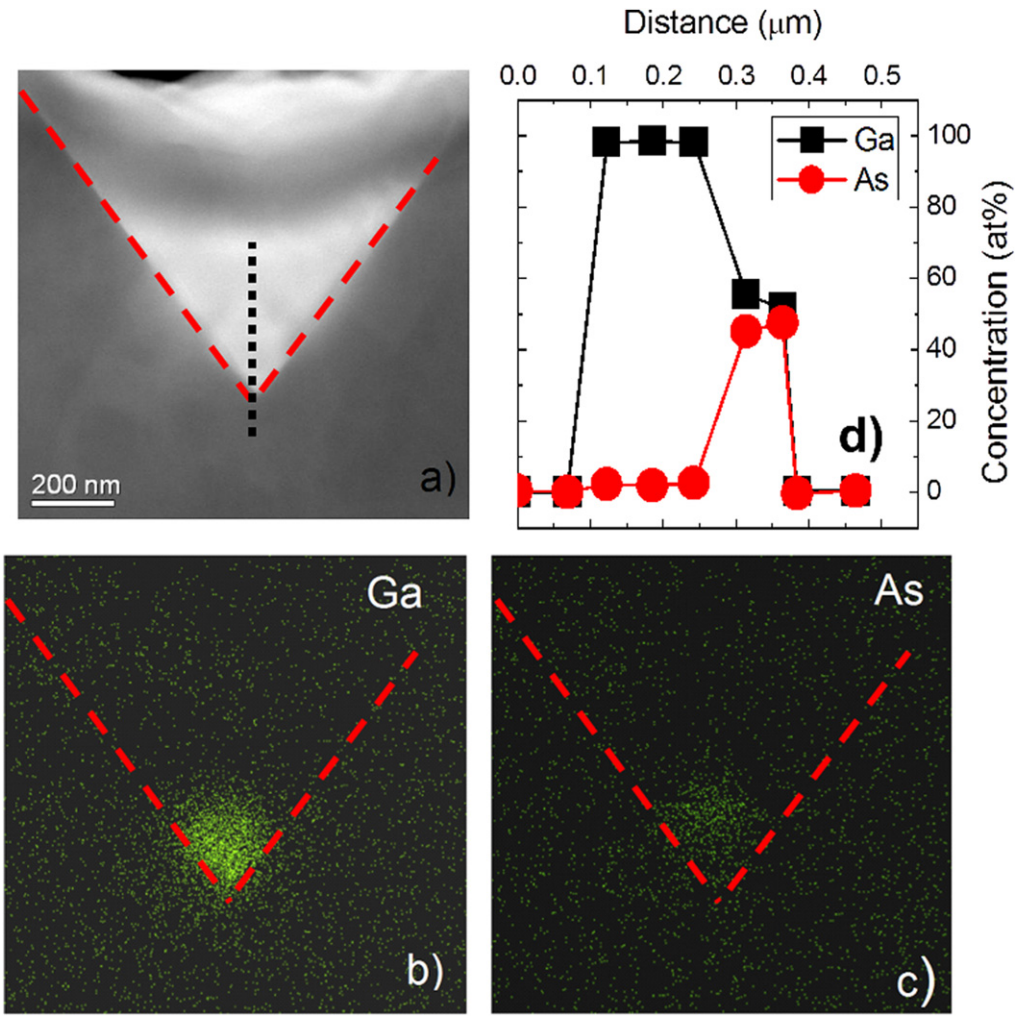

Figure 4. STEM-HAADF image (a) and EDX Ga and As elemental maps (b)–(c) of a Ga droplet in a {111} pyramidal silicon pit after As irradiation. The red dashed lines mark the Si pit profile. The absolute Ga (black) and As (red) concentrations (at%) are shown in panel (d), as calculated from spectra taken across the deposited material starting at the bottom of the pit, along the black dotted line in (a) (see text).

the Mullins–Sekerka instability outlined in Reyes *et al.* This instability is magnified in the present system due to the influx of As arriving along the Si surface by diffusion. The unstable growth mode implies an accelerated growth of GaAs along the Ga-vapor interface, resulting in the observed GaAs shell.

As a consequence of this nucleation-induced growth mode, incomplete crystallization is naturally favored. Increased As flux promotes more growth at the liquid–vapor interface rather than penetration into the liquid core. Decreased As flux results in a longer time scale for growth, which can allow for the nucleation of GaAs away from the triple-point provided that the incubation time for GaAs nucleation on Si can be realized [41]. Such nucleation sites away from the triple junction can serve to more fully crystallize the droplet or increase the characteristic length scale of the GaAs shell. The droplet may be fully crystallized only if its height is consistent with this length scale. Embedding smaller Ga NPs can be achieved by decreasing the Ga droplet volume and counterbalancing this reduction of length scale with an increase of the As flux during the crystallization process. The KMC results therefore make it possible to introduce a scaling law for the production of embedded NPs of the desired size, thus allowing for a fine tuning of the LSPR to the energy required for the specific application.

In conclusion, we demonstrate the possibility to fabricate uniform, ordered arrays of embedded Ga NPs on Si substrates. The growth process strongly relies on interplay of: (i) the Si substrate patterning, in form of a periodically modulated two dimensional inverted pyramid pit array, in order to promote NP ordering; (ii) the deposition of Ga in an MBE environment in the form of droplets which can be successfully trapped at the bottom of the pits due to the combined effects of capillarity condensation and nucleation kinetics; (iii) the crystallization of the Ga droplets under As flux. The latter, due to the combined effects of pit geometry and direction dependent growth velocities, permits the formation of a GaAs cap confined to the liquid–vapor interface, thus resulting in the embedding of a Ga NP. The patterning process is based on standard nano-lithographic technique, and it therefore fully scalable. The pit arrangement, in terms of topology, pit distance and depth, is fully designable. This permits the fabrication on purpose of arrays which will allow for a fine tuning

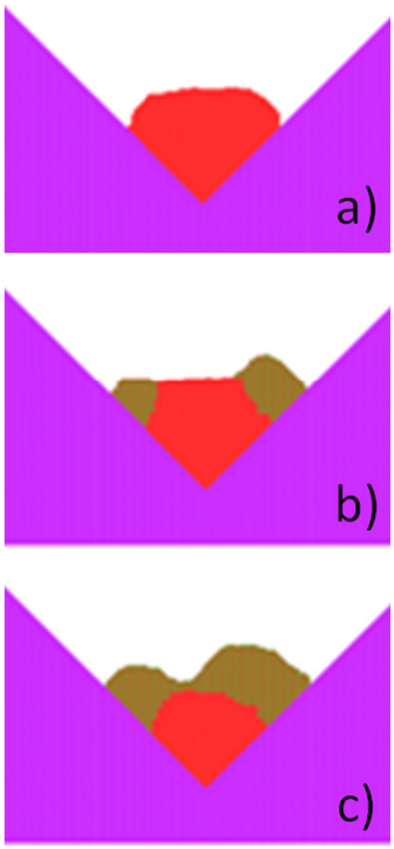

Figure 5. KMC simulated crystallization results. Three simulation snapshots are reported: (a) after Ga deposition, in which a Ga droplet has formed; (b) during exposure to the As flux, in which GaAs at the vapor–liquid–solid intersection; (c) At the end of crystallization in which a Ga NP covered by a thin GaAs layer has been obtained. Color codes are purple for Si, red for Ga and brown for GaAs, respectively.

of the plasmonic properties, thus opening a wide range of design possibilities for absorption enhancement of semiconductors via LSPR-enhanced scattering and internal photoemission strategies.

The research was supported in Italy by the CARIPLO Foundation (EIDOS—no. 2011-0382). The technical and scientific support of the staff at the ID13 beamline of the European Synchrotron Radiation Facility, Grenoble, is gratefully acknowledged (experiment SI-2057). P S and K R were supported, in part, by NSF support grants DMS-0810113, DMS-0854870, and DMS-1115252.

References

[1] Bohren C F and Huffman D R 2008 *Absorption and Scattering of Light by Small Particles* (New York: Wiley)
[2] Atwater H A and Polman A 2010 Plasmonics for improved photovoltaic devices *Nat. Mater.* **9** 205–13
[3] Green M A and Pillai S 2012 Harnessing plasmonics for solar cells *Nat. Photonics* **6** 130
[4] Polman A 2008 Plasmonics applied *Science* **322** 868–9
[5] Catchpole K R and Polman A 2008 Plasmonic solar cells *Opt. Express* **16** 21793–800
[6] Nishijima Y, Ueno K, Yokota Y, Murakoshi K and Misawa H 2010 Plasmon-assisted photocurrent generation from visible to near-infrared wavelength using a Au-nanorods/TiO_2 electrode *J. Phys. Chem. Lett.* **1** 2031–6
[7] Takahashi Y and Tatsuma T 2011 Solid state photovoltaic cells based on localized surface plasmon-induced charge separation *Appl. Phys. Lett.* **99** 182110
[8] Wang F and Melosh N A 2011 Plasmonic energy collection through hot carrier extraction *Nano Lett.* **11** 5426–30
[9] Knight M W, Sobhani H, Nordlander P and Halas N J 2011 Photodetection with active optical antennas *Science* **332** 702–4
[10] Dunbar R B, Pfadler T and Schmidt-Mende L 2012 Highly absorbing solar cells–a survey of plasmonic nanostructures *Opt. Express* **20** A177–89
[11] Albella P, Garcia-Cueto B, Gonza lez F, Moreno F, Wu P C, Kim T-H, Brown A, Yang Y, Everitt H O and Videen G 2011 Shape matters: plasmonic nanoparticle shape enhances interaction with dielectric substrate *Nano Lett.* **11** 3531–7
[12] Zhu S, Chu H S, Lo G Q, Bai P and Kwong D L 2012 Waveguide-integrated near-infrared detector with self-assembled metal silicide nanoparticles embedded in a silicon p-n junction *Appl. Phys. Lett.* **100** 061109
[13] Barnes W, Dereux A and Ebbesen T 2003 Surface plasmon subwavelength optics *Nature* **424** 824–30
[14] Henzie J, Lee M H and Odom T W 2007 Multiscale patterning of plasmonic metamaterials *Nat. Nanotechnology* **2** 549–54
[15] Cattoni A, Ghenuche P, Decanini D, Chen J, Pelouard J and Collin S 2011 λ^3/1000 plasmonic nanocavities for biosensing fabricated by soft UV nanoimprint lithography *Nano Lett.* **11** 3557–63
[16] Giermann A L and Thompson C V 2005 Solid-state dewetting for ordered arrays of crystallographically oriented metal particles *Appl. Phys. Lett.* **86** 121903
[17] Choi W K *et al* 2008 A combined top-down and bottom-up approach for precise placement of metal nanoparticles on silicon *Small* **4** 330–3
[18] Tonova D, Patrini M and Tognini P 1999 Ellipsometric study of optical properties of liquid Ga nanoparticles *J. Phys. Condens. Matter* **11** 2211
[19] Tognini P, Stella A, Cheyssac P and Kofman R 1999 Surface plasma resonance in solid and liquid Ga nanoparticles *J. Non-Cryst. Solids* **249** 117–22
[20] Spirkoska D *et al* 2009 Structural and optical properties of high quality zinc-blende/wurtzite GaAs nanowire heterostructures *Phys. Rev.* B **80** 1–9
[21] Wu P C, Kim T-H, Brown A S, Losurdo M, Bruno G and Everitt H O 2007 Real-time plasmon resonance tuning of liquid Ga nanoparticles by *in situ* spectroscopic ellipsometry *Appl. Phys. Lett.* **90** 103119
[22] Kang M, Saucer T W, Warren M V, Wu J H, Sun H, Sih V and Goldman R S 2012 Surface plasmon resonances of Ga nanoparticle arrays *Appl. Phys. Lett.* **101** 081905
[23] Koguchi N, Takahashi S and Chikyow T 1991 New MBE growth method for InSb quantum well boxes *J. Cryst. Growth* **111** 688
[24] Sanguinetti S and Koguchi N 2013 Droplet epitaxy of nanostructures *Molecular Beam Epitaxy From Research to Mass Production* ed M Henini (Amsterdam: Elsevier) p 95
[25] Mano T, Mitsuishi K, Nakayama Y, Noda T and Sakoda K 2008 Structural properties of GaAs nanostructures formed by a supply of intense As4 flux in droplet epitaxy *Appl. Surf. Sci.* **254** 7770–3
[26] Reyes K, Smereka P, Nothern D, Millunchick J M, Bietti S, Somaschini C, Sanguinetti S and Frigeri C 2013 Unified model of droplet epitaxy for compound semiconductor nanostructures: experiments and theory *Phys. Rev.* B **87** 165406

[27] Lee E H, Song J D, Yoon J J, Bae M H, Han I K, Choi W J, Chang S K, Kim Y D and Kim J S 2013 Formation of self-assembled large droplet-epitaxial GaAs islands for the application to reduced reflection *J. Appl. Phys.* **113** 154308
[28] Bietti S, Somaschini C, Koguchi N, Frigeri C and Sanguinetti S 2010 Self-assembled local artificial substrates of GaAs on Si substrate *Nanoscale Res. Lett.* **5** 1905
[29] Somaschini C, Bietti S, Koguchi N, Montalenti F, Frigeri C and Sanguinetti S 2010 Self-assembled GaAs islands on Si by droplet epitaxy *Appl. Phys. Lett.* **97** 053101
[30] Zhong Z and Bauer G 2004 Site-controlled and size-homogeneous Ge islands on prepatterned Si (001) substrates *Appl. Phys. Lett.* **84** 1922
[31] Gallo P, Felici M, Dwir B, Atlasov K A, Karlsson K F, Rudra A, Mohan A, Biasiol G, Sorba L and Kapon E 2008 Integration of site-controlled pyramidal quantum dots and photonic crystal membrane cavities *Appl. Phys. Lett.* **92** 263101
[32] Bollani M, Chrastina D, Montuori V, Terziotti D, Bonera E, Vanacore G M, Tagliaferri A, Sordan R, Spinella C and Nicotra G 2012 Homogeneity of Ge-rich nanostructures as characterized by chemical etching and transmission electron microscopy *Nanotechnology* **23** 045302
[33] Sato K, Shikida M, Yamashiro T, Asaumi K, Iriye Y and Yamamoto M 1999 Anisotropic etching rates of single-crystal silicon for TMAH water solution as a function of crystallographic orientation *Sensors Actuat.* A **73** 131
[34] Mutaftschiev B 2001 *The Atomistic Nature of Crystal Growth* (Berlin: Springer)
[35] Venables J A, Spiller G D T and Hanbuenchen M 1984 Nucleation and growth of thin films *Rep. Prog. Phys* **47** 399
[36] Kim J S, Jeong M S, Byeon C C, Ko D-K, Lee J, Kim J S, Kim I-S and Koguchi N 2006 GaAs quantum dots with a high density on a GaAs (111)A substrate *Appl. Phys. Lett.* **88** 072107
[37] Mulheran P and Basham M 2008 Kinetic phase diagram for island nucleation and growth during homoepitaxy *Phys. Rev.* B **77** 075427
[38] Chrastina D, Vanacore G M, Bollani M, Boye P, Schöder S, Burghammer M, Sordan R, Isella G, Zani M and Tagliaferri A 2012 Patterning-induced strain relief in single lithographic SiGe nanostructures studied by nanobeam x-ray diffraction *Nanotechnology* **23** 155702
[39] Henke B L, Gullikson E M and Davis J C 1993 X-Ray interactions: photoabsorption, scattering, transmission and reflection at E = 50–30 000 eV, Z = 1–92 *At. Data Nucl. Data Tables* **54** 181
[40] Krause M O, Nestor C W J, Sparks C J and Ricci E 1978 X-ray fluorescence cross sections for K and L x-rays of the elements *Oak Ridge National Laboratory Report* 5399
[41] DeJarld M, Reyes K, Smereka P and Millunchick J M 2013 Mechanisms of ring and island formation in lattice mismatched droplet epitaxy *Appl. Phys. Lett.* **102** 133107